Nano Energy 131 (2024) 110276

Contents lists available at ScienceDirect

Nano Energy

journal homepage: www.elsevier.com/locate/nanoen

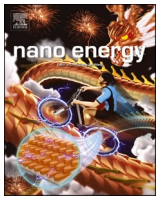

Ultra-high rate performance of single-crystalline NMC cathodes enabled by a TEP-based electrolyte

Lingli Chen [a], Biwei Xiao [b,*], Weibin Chen [a], Pengtao Zhang [a], Tao Huang [a], Weiyuan Huang [b], Zhencheng Huang [a], Qingyun Lin [d], Pei Liu [a], Xuanlong He [a], Yuying Liu [a], Haoran Wei [a], Shenghua Ye [a], Liewu Li [a], Jing Chen [e], Xuming Yang [a], Xiangzhong Ren [a], Xiaoping Ouyang [a,e], Jianhong Liu [a,f], Feng Pan [c,*], Qianling Zhang [a,*], Jiangtao Hu [a,*]

[a] Graphene Composite Research Center, College of Chemistry and Environmental Engineering, Shenzhen University, Shenzhen 518060, PR China
[b] GRINM (Guangdong) Research Institute for Advanced Materials and Technology, Foshan, Guangdong 528051, PR China
[c] School of Advanced Materials Shenzhen Graduate School, Peking University, Shenzhen 518060, PR China
[d] Center of Electron Microscopy, State Key Laboratory of Silicon and Advanced Semiconductor Materials, School of Materials Science and Engineering, Zhejiang University, Hangzhou 310027, PR China
[e] School of Materials Science and Engineering, Xiangtan University, Xiangtan 411105, PR China
[f] Shenzhen Eigen-Equation Graphene Technology Co., Ltd, Shenzhen 518000, PR China

ARTICLE INFO

Keywords:
Single crystal Ni-rich cathode
Solvation sheath
Fast interfacial kinetics
Cathode-electrolyte interphase
Flame-retardant

ABSTRACT

Harnessing the full potential of Ni-rich single-crystal cathodes ($LiNi_xMn_yCo_{1-x-y}O_2$, NMC) for next-generation high-energy lithium batteries is hindered by their slow reaction kinetics and susceptibility to interfacial decay. Our research introduces a novel strategy utilizing triethyl phosphate (TEP) and fluoroethylene carbonate (FEC) to optimize the Li^+ solvation environment, lowering the coordination number and diminishing the energy threshold for Li^+ transport. Mechanistic studies indicate that this intervention not only accelerates the Li^+ transfer at the electrode/electrolyte interface but also catalyzes the development of a robust LiF-rich CEI layer. As a result, the single-crystal NMC83 cathode exhibits remarkable high-rate discharge capacities of approximately 209 mAh g^{-1} at 0.1 C and 192 mAh g^{-1} at 0.5 C. The robust CEI layer also mitigates parasitic reactions, substantially improving the cycle life, with capacity retention increasing from 46.1 % to 88.2 % after 300 cycles at 1 C. This work underscores the transformative impact of solvation sheath engineering on the interfacial dynamics of single-crystal cathodes, paving the way for more durable and efficient energy storage solutions.

1. Introduction

Lithium-ion batteries (LIBs) are the preferred power source for portable electronic devices, electric vehicles, stationary energy storage systems and grid applications due to their exceptional energy density and extended lifespan [1,2]. However, the advancements in LIBs are challenged by the need for superior rate performance, wider operating temperature, and enhanced safety [3]. Notably, Ni-rich layered oxides, specifically $LiNi_xMn_yCo_{1-x-y}O_2$ (NMC) with ≥80 % Ni, are favored for their high theoretical capacity and high operating voltage [4–7]. Polycrystalline Ni-rich cathodes are prone to intergranular microcracking during electrochemical cycling due to lattice anisotropic strain and phase transformations, which leads to capacity fade and structural degradation [8,9]. In contrast, single-crystal Ni-rich cathodes exhibit enhanced structural integrity and thermal stability due to the absence of grain boundaries and uniform lattice orientation, thereby reducing intergranular microcrack and gas evolution [10–12]. However, the micro-sized single-crystal materials present elongated ion diffusion pathways, resulting in sluggish Li^+ transport kinetics.

To enhance the electrochemical performance of NMC cathodes, researchers have employed various strategies, including elemental doping [13–15], surface coating [16–18], electrolyte screening [19,20], etc. Elemental doping and surface coating can mitigate the intrinsic evolution of anisotropic lattice parameters in layered oxides, enhancing the material's cycle stability. However, this approach may encounter the challenges of sacrificed initial capacity, reduced rate-retention as well as increased material cost [14,18]. Consequently, the focus of research has shifted towards electrolyte engineering due to the intricate nature of

* Corresponding authors.
E-mail addresses: xiaobiwei@grinm.com (B. Xiao), panfeng@pkusz.edu.cn (F. Pan), zhql@szu.edu.cn (Q. Zhang), hujt@szu.edu.cn (J. Hu).

https://doi.org/10.1016/j.nanoen.2024.110276
Received 15 August 2024; Received in revised form 10 September 2024; Accepted 17 September 2024
Available online 20 September 2024

material modification and associated adverse effects. Traditional electrolytes can now be designed to align with the specific demands of battery systems [21,22]. Initially, incorporating additives into conventional carbonated-based electrolytes has significantly bolstered both the initial capacity and rate performance, by establishing a compact and stable cathode electrolyte interphase (CEI) [23]. Secondly, the careful selection and blending of solvents have also been demonstrated to supplement the Li^+ migration mechanism [24,25]. For example, Fan et al.[26] have successfully utilized small molecular solvents to reduce the energy barrier for Li^+ transport, offering a novel design of electrolytes for rapid charge-discharge cycling. Moreover, in light of the suboptimal thermal stability associated with $LiPF_6$, researchers have revisited the selection of lithium salts and the optimization of their concentrations [27,28]. In general, the development of a new electrolyte, particularly for single-crystal materials, aims to form a dense and stable CEI while simultaneously ensuring that Li-ions encounter minimal energy barriers during solvation/desolvation and diffusion across the interface.

Ensuring superior safety is imperative for the widespread adoption of batteries in the consumer electronics market. However, utilizing flammable organic electrolyte poses a challenge to manufacturing high-safety batteries. Therefore, the research of non-flammable or flame-retardant electrolytes is becoming increasingly important [29]. Phosphorus-based solvents offer excellent thermal stability and have the ability to form a protective layer that safeguards against oxygen and heat effects [30,31]. Specifically, triethyl phosphate (TEP) has been studied extensively due to its advantageous properties, including a wide operational temperature range, great lithium salt solubility, low viscosity, and low melting point [32]. However, TEP-based electrolyte often suffers from reduced cycle stability. This is attributed to the unstable CEI, resulting in continuous electrolyte consumption [33]. Consequently, it is imperative to conduct a thorough screening of an adjuvant in order to mitigate the adverse effects of TEP and notably enhance battery safety.

Here, a flame-retardant electrolyte was developed using $LiBF_4$ as the lithium salt, TEP and fluoroethylene carbonate (FEC) as solvents, supplemented with a small amount of lithium difluorophosphate (LiDFP) as an additive. Compared to traditional electrolyte, this electrolyte system effectively promotes a dense LiF-rich CEI layer at the electrode-electrolyte interface, resulting in enhanced cycle retention (88.2 %

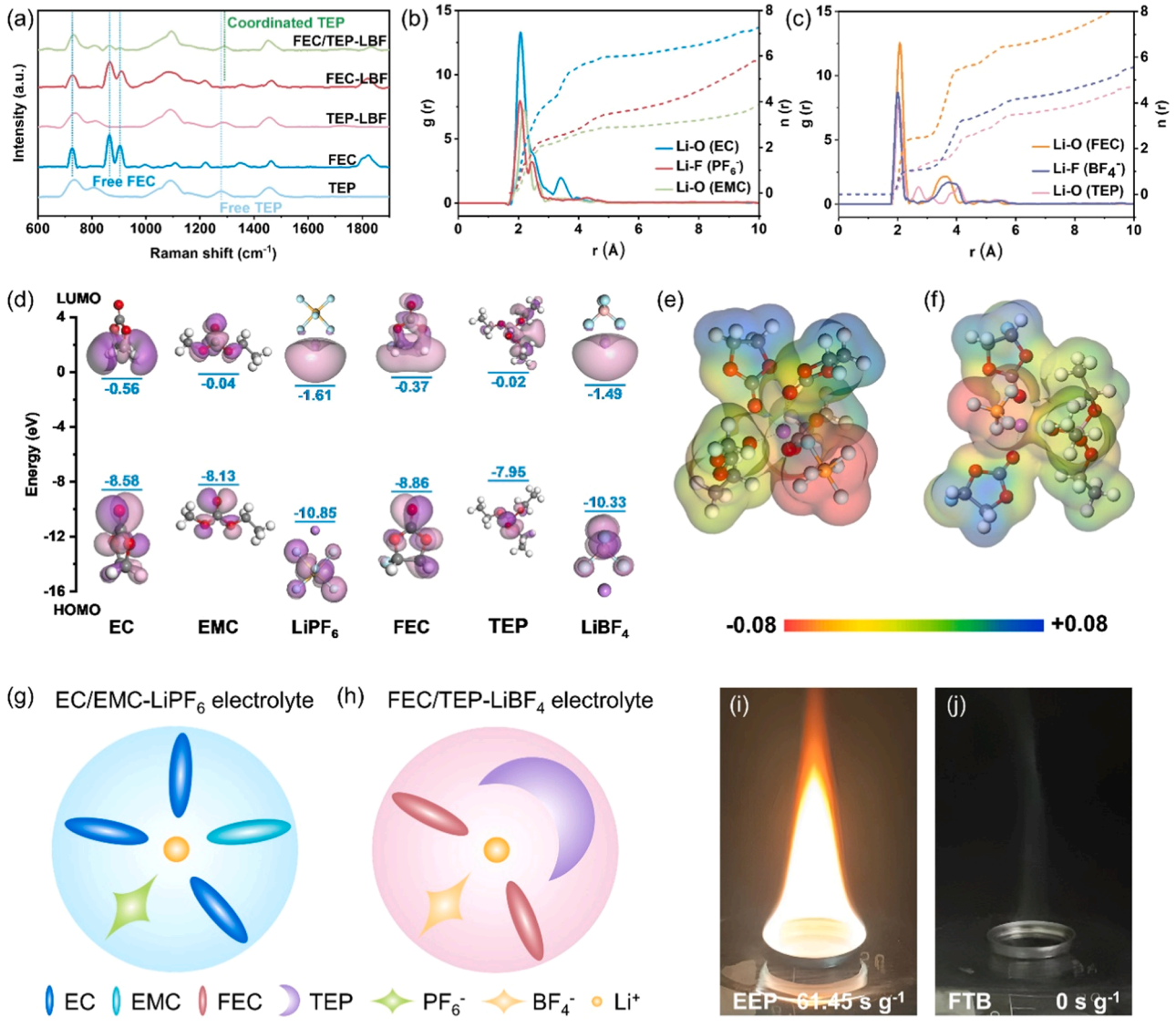

Fig. 1. Characterizations of the designed electrolytes. (a) Raman spectra of the utilized solvents and electrolytes. (b,c) RDF and coordination number with Li^+ calculated in different electrolytes. (d) The molecular orbital energy (LUMO and HOMO) of the applied solvents and lithium salts. (e,f) Electrostatic potential (ESP) for the solvation structure of EC/EMC-$LiPF_6$ (e) and FEC/TEP-$LiBF_4$ (f). (g,h) Schematic diagram of solvation structure of EC/EMC-$LiPF_6$ (g) and FEC/TEP-$LiBF_4$ (h). (i,j) Ignition tests of the glass fiber after immersed in EEP (i) and FTB (j).

after 300 cycles). Furthermore, the rate capability of single-crystal NMC83 cathode is also enhanced, presenting 209.3 mAh g^{-1} high reversible capacity at 0.1 C and 191.8 mAh g^{-1} at 0.5 C, respectively. Theoretical calculations demonstrate that the designed electrolyte effectively modifies the solvent shell structure of Li^+, leading to a reduction in the coordination number of the first shell due to the incorporation of macromolecule TEP. This modification significantly decreases the desolvation energy of lithium ions, facilitating their rapid transmission at interfaces and enhancing the magnification performance of single crystal materials. The electrolyte engineering technique offers novel insights for the development of high-performance single-crystal NMC cathodes.

2. Results and discussion

2.1. Electrolyte characterization

Raman spectroscopy (Fig. 1a) was utilized to scrutinize the influence of TEP and FEC on the electrolyte's solvation structure. Notably, the pure FEC solvent displayed three distinct absorption bands at 727 cm^{-1}, 865 cm^{-1}, and 906 cm^{-1} The pure TEP manifested a broad peak at approximately 1279 cm^{-1}, which corresponds to the stretching vibration of the unbounded P═O bond within TEP molecules [34]. Within the FEC/TEP-LBF electrolyte (1.5 M $LiBF_4$ in FEC/TEP), this broad peak underwent a shift to a higher wavenumber of 1289 cm^{-1}, suggesting an intensification of Li^+ solvation by TEP. This shift, when juxtaposed with the peak position of 1287 cm^{-1} in the TEP-$LiBF_4$ electrolyte, implies that the incorporation of FEC does not substantially modify the solvation environment surrounding TEP molecules. The two bands related to FEC were observed to have shifted to 732 cm^{-1} and 904 cm^{-1}, respectively [35], signifying a preferential occupation of the first solvation shell of Li^+ by FEC solvent molecule.

To gain further theoretical insights into the solvation structure of FEC/TEP-LBF electrolyte, molecular dynamics (MD) simulations were executed. The outcomes pertaining to the radial distribution function (g (r)) and coordination number (n(r)) are delineated with continuous and intermittent lines, respectively. Within the EC/EMC-1 M $LiPF_6$ electrolytic system (Fig. 1b), Li^+ continues to be predominantly encircled by EC and PF_6^-, occupying the primary solvation shell. Parallel observations are noted in the FEC/TEP-LBF electrolytic matrix (Fig. 1c), albeit with a discernible variance. The complement of solvent molecules coordinated to Li^+ is considerably diminished, concomitant with a reduction in the dimensions of the initial solvation shell. To expound with specificity, in the EC/EMC-1 M $LiPF_6$ context, the number of EC, EMC, molecules, and PF_6^- anions in the first shell is 3.0, 1.7, and 1.8. Contrastingly, within the FEC/TEP-LBF electrolyte system, the number of molecules of FEC, TEP and BF_4^- anions is 2.3, 1.3 and 1.2. The diminished n(r) indicates that within the FEC/TEP-LBF electrolyte system, the steric hindrance effect of TEP molecules impedes the coordination of other solvent molecules and BF_4^- anions, thereby facilitating the desolvation process of Li^+. To augment the understanding of the decomposition dynamics of solvent and solute molecules during electrochemical processes, the HOMO and LUMO energy levels were calculated (Fig. 1d). It is observed that the LUMO of EC, EMC, and $LiPF_6$ are positioned below their respective counterparts, suggesting a propensity for reduction. Conversely, at the HOMO level, TEP and $LiBF_4$ exhibit higher energy levels relative to their respective molecules, indicating a greater susceptibility to oxidation. In addition, the electrostatic potential diagram (MEP) calculated by DFT confirms that the solvated shells in the two electrolytic media have a similar MEP range (Fig. 1e, f). Figs. 1g and 1h succinctly outline the Li^+ solvation structures for two types of electrolytes. The EC/EMC-$LiPF_6$ formulation includes 3 EC, 1 EMC, and 1 PF_6^-, which is more than the coordination number found in the FEC/TEP-$LiBF_4$ system, comprising 2 FEC molecules, 1 TEP, and 1 BF_4^-. The observed decrease in n(r) for the FEC/TEP-LBF electrolyte system can be attributed to the steric interference of TEP molecules, which impedes the coordination of adjacent solvents with BF_4^- anions. Consequently, this diminishment in solvent coordination facilitates the desolvation of Li^+ and enhances its ionic mobility by lowering the energetic barrier for solvent molecule displacement.

In order to validate the safety profiles of 1.5 M $LiBF_4$ in FEC/TEP (1:3 by vol.) with 0.1 % $LiPF_2O_2$ (FTB) and 1 M $LiPF_6$ in EC/EMC (3:7 by vol.) with 2 % VC (EEP), ignition tests [36] were meticulously carried out (Fig. 1i, j). The EEP electrolyte, which is combustible, has the ability to sustain combustion for more than 7 seconds, with an associated SET (Self-extinguishing time) reaching a significant value of 61.45 s g^{-1} (Video S1). Conversely, the FTB electrolyte has been demonstrated to significantly diminish combustibility, consistently thwarting combustion in repeated ignition tests (Videos S2). To advance the evaluation of TEP's flame retardant properties, an assay was devised to gauge the influence of diverse electrolytes on the combustion resistance of glass fibers, as illustrated in Fig. S1 and Table S1. Notably, the glass fibers treated with the FEC-based electrolyte displayed the most intense charring. In stark contrast, electrolytes formulated with TEP, showed reduced thermal reactivity, underscoring the capacity to attenuate the thermal hazards inherent in electrolytic systems.

2.2. Electrochemical evaluation of the designed electrolytes

The initial charge-discharge voltage profiles of single-crystal NMC83 tested in EEP and FTB were illustrated in Fig. 2a. Notably, under 0.1 C, FTB-based cell demonstrates a superior discharge specific capacity (209.3 mAh g^{-1}), effectively engaging a greater amount of recyclable active Li^+. This enhanced performance is credited to both the elevated charge specific capacity (237.5 mAh g^{-1}) and the Coulombic efficiency (88.1 %). After 100 cycles, the FTB-based cell preserves a more reversible H2-H3 phase transition, discernible through the attenuation in redox peak intensity (Fig. S2a, b). A quantitative evaluation of the retained peak area indicates that the FTB-based cell exhibits a mere 0.04 % reduction, indicating its exceptional reversibility (Fig. S2c). Despite the initial similarity in Coulombic efficiency of the two electrolytes, the EEP-based cell shows a capacity retention of only 46.1 % and 48.2 % after 300 cycles at 1 C and 2 C, respectively (Fig. 2b and S3). This is attributed to a notable increase in polarization (Fig. S4). In contrast, under identical conditions, the FTB-based cells display an ultra-stable cycling, maintaining 88.2 % and 87.3 %. The charge-discharge curves further corroborate that the FTB-based cell is adept at minimizing voltage decay (Fig. 2c). Additionally, to substantiate the thermal stability, extended cycle tests were executed at 45 °C (Fig. 2d). The FTB-based cell retains a remarkable 81.3 % of its initial capacity after 200 cycles, in sharp contrast to the precipitous capacity decline exhibited by the EEP-based cell. To explore the practical application of flame-retardant electrolytes, the full cell was assembled with a high-loading cathode (29 mg cm^{-2}) and a silicon-carbon anode (4.23 mg cm^{-2}), with a cutoff voltage of 4.25 V. As shown in Fig. S5, the full cell with FTB exhibited excellent cycle stability over 200 cycles, retaining 89.0 % of its capacity with an average high Coulombic efficiency of over 99.8 %. The limited polarization throughout the entire cycle further indicates stable electrodes and efficient Li^+ transport through the electrolyte/electrode interface. Additionally, examining the Coulombic efficiency across cycles reveals that FTB maintains higher and more stable CE than EEP, indicating improved reversibility in Li|| NMC83 battery systems. An in-depth analysis of the rate capability reveals that the FTB-based cell consistently outperforms the EEP-based cell across a spectrum of current densities (Fig. 2e). This superiority is likely attributed to the FTB electrolyte's proficiency in increasing interfacial ionic dynamics, thereby ensuring a more potent energy conversion efficiency. To the best of our knowledge(Fig. 2f and Table S2), this work using TEP-based electrolyte has surpassed most of the other reported studies [37–46].

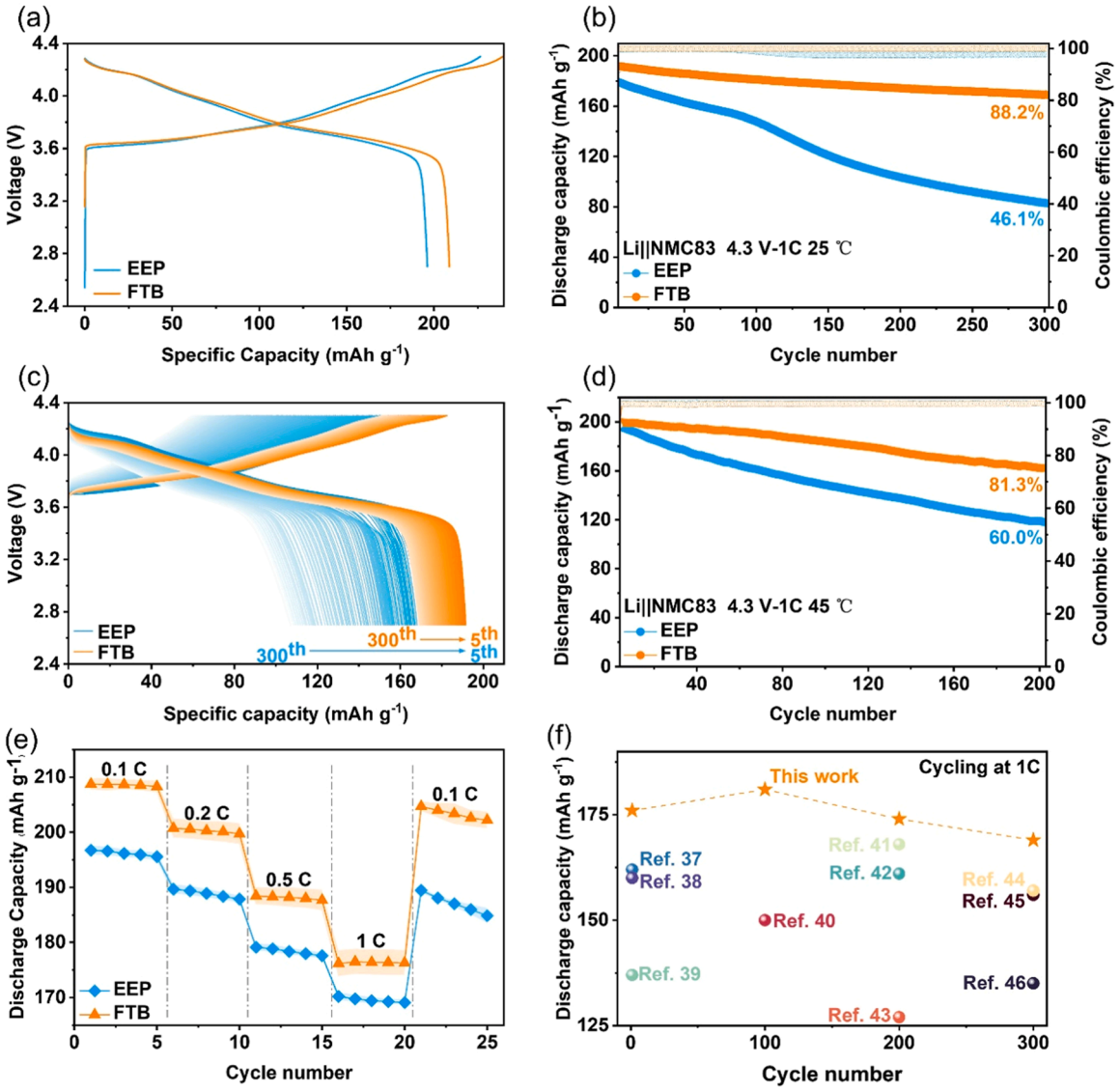

Fig. 2. Electrochemical performances of Li||NMC83 cells. (a) Initial charge/discharge curves of single-crystal NMC83 cathode with a cutoff voltage of 4.3 V. (b) Cycle stability performance of Li||NMC83 half cells in EEP and FTB. (c) Corresponding charge/discharge profiles from the 5th to 300th cycles. (d) Cycling performance of Li||NMC83 cells cycled at 45 ℃. (e) Rate capability of Li||NMC83 cells tested in the EEP and FTB. (f) Comparison of initial discharge capacity and cycling performance of 1 C for NMC83 in this work with representative reports.

2.3. Post-cycling microscopy and structural characterization of single-crystal NMC83

Structural instability stands as a primary culprit for the rapid capacity fade observed over extended cycles, underscoring the necessity to investigate the degradation of the NMC83 cathode. Initially, in-situ X-ray diffraction (XRD) was deployed to monitor the crystal structure's real-time evolution, with a meticulous examination of the specific diffraction peaks within the NMC83 cathode (Fig. S6). Specifically, during the extraction of Li^+ ranging from 2.7 V to 4.0 V, the (003) diffraction peak shifts toward a lower angle, signifying an expansion of the interlayer spacing and an intensified repulsion between oxygen layers. This phenomenon can incubate intense stress concentration, nucleating microcracks within the particles and culminating in structural disintegration [47]. Encouragingly, within the FTB-based NMC83, the characteristic (003) peak transition from the H2 phase to the H3 phase is markedly subdued, with a total angular deviation of merely 0.71°, in contrast to the more pronounced shift observed in the EEP-based cathode. Similar trends are observed for the (102) and (104) diffraction peaks, further substantiating the stabilizing influence of the FTB-based NMC83 on the cathode's crystal structure. Secondly, after 100 cycles, the XRD patterns reveal that the (003) peak for the EEP-based NMC83 has shifted obviously to a lower angle (Fig. 3a, b). This shift indicated lattice expansion along the c-axis due to the irreversible loss of Li^+ and increased repulsion among oxygen atoms. This is accompanied by reduced peak intensity and broadening, suggesting structural instability. In contrast, the FTB-based NMC83 maintains peak stability, reflecting its robust crystal structure under high-voltage cycling [48,49].

To substantiate the single-crystal morphology's integrity, pristine and cycled electrodes were examined using scanning electron microscopy (SEM) (Fig. 3c, d and S7). After 100 cycles, the secondary particles tested in EEP electrolyte exhibited noticeable cracks and delamination. In contrast, the single-crystal structure of NMC83 particles in the FTB electrolyte remained intact. This is primarily attributed to the CEI layer facilitated by the FTB electrolyte, which provides additional mechanical support for the cathode and mitigates the propagation of micro-cracks during the cycling process [48]. The surface structure of single-crystal

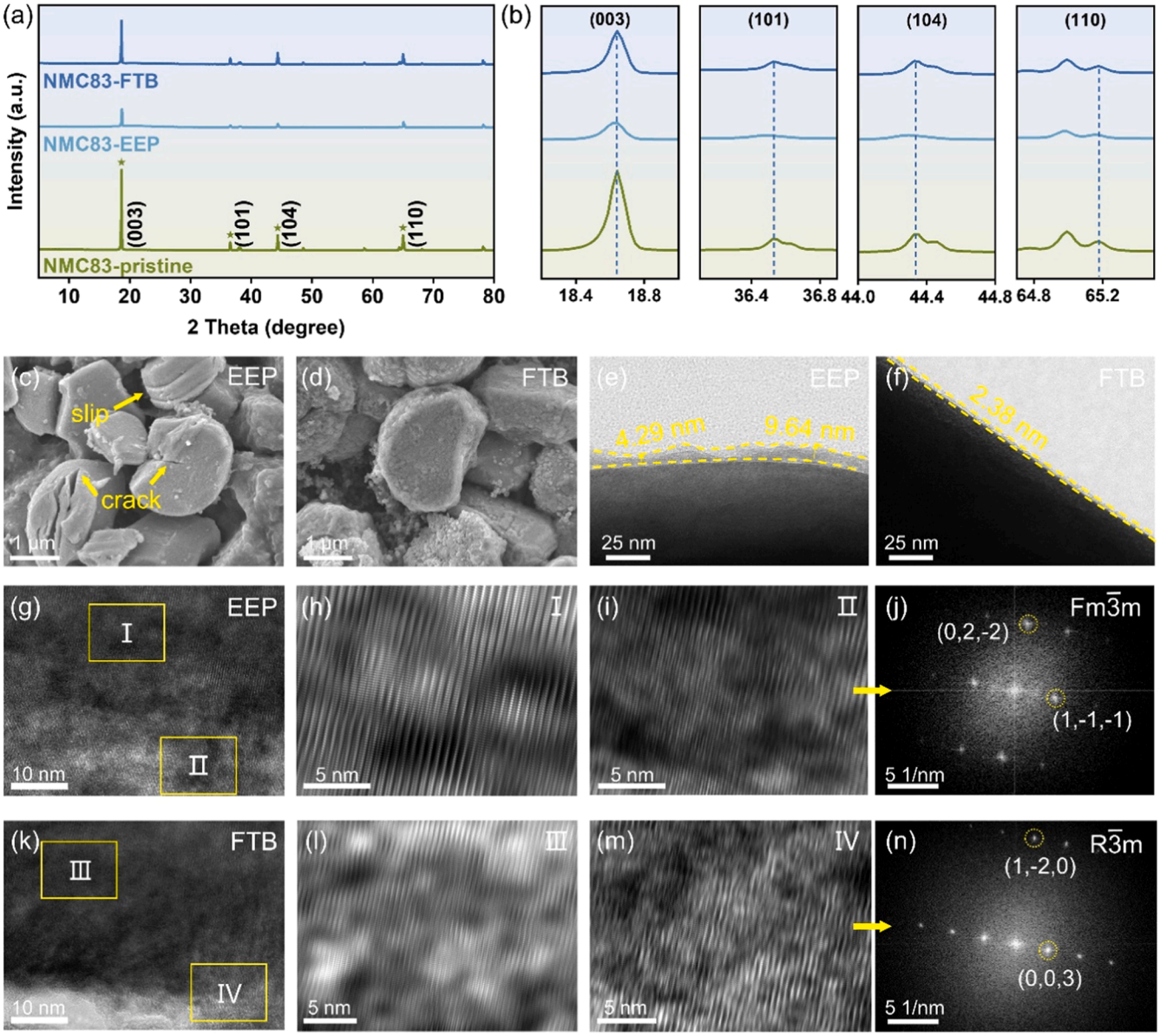

Fig. 3. Characterizations of single crystal NMC83 cathode. (a,b) XRD patterns of pristine and cycled NMC83 cathodes in EEP and FTB electrolytes. SEM images of 100-cycled NMC83 cathodes in EEP (c) and FTB (d). TEM images of the CEI layers formed in EEP (e) and FTB (f). HRTEM images of single-crystal NMC83 after 100 cycles in EEP (g-j) and FTB (k-n).

NMC83 particles were further characterized by TEM (Transmission Electron Microscopy). When coupled with EEP electrolyte, irregular CEI films with thicknesses varying from 4.29 to 9.64 nm were observed on the surface of NMC83 (Fig. 3e, f). Moreover, the magnified image at site II in Fig. 3g was identified as a typical rock-salt phase, stemming from the intermixed arrangement of Li^{+}/Ni^{2+} during delithiation/lithiation (Fig. 3h-j) [50]. Comparatively, the CEI film formed under FTB-based was significantly denser and thinner (≈ 2.38 nm). It nearly retained the original layered structure (Fig. 3k-n). It can be deduced that the FTB electrolyte aids in curbing parasitic side reactions. The CEI layer formed is instrumental in preserving the single-crystal particle surface and bulk integrity over prolonged cycling, featuring reversible structural transitions.

2.4. Interfacial analysis of the cycled single-crystal NMC83

To further elucidate the impact of the designed electrolyte on single-crystal NMC83 cathode, a meticulous surface chemical analysis was carried out using Time-of-Flight Secondary Ion Mass Spectrometry (TOF-SIMS). The findings revealed that the distinctive signals of LiF_2^- and F^- were significantly more pronounced in the FTB electrolyte (Fig. 4a and S8a). which may be attributed to F-contained species, like $LiPO_2F_2$[19]. Moreover, the FTB electrolyte exhibited a diminished signal for organic decomposition products on the electrode surface, indicating reduced electrolyte degradation and thereby contributing to the preservation of interface integrity and ionic transport efficiency [51]. This observation is corroborated by the TOF-SIMS 2D and 3D mapping images (Fig. 4b-h and S8b-h). Conversely, EEP-based electrode revealed a higher presence of organic decomposition products, exemplified by C_2HO^-, LiH_2O^-, and signals associated with the decomposition of lithium salts, such as PO_2^-, PO_3^-[52]. The detection of these species is indicative of exacerbated electrolyte decomposition, culminating in the formation of a thicker and less uniform CEI film. In pursuit of a more profound understanding of the CEI's detailed structure as formed in the distinct electrolytes, an XPS etching analysis was conducted on the cycled samples. This involved progressively sputtering argon ions from

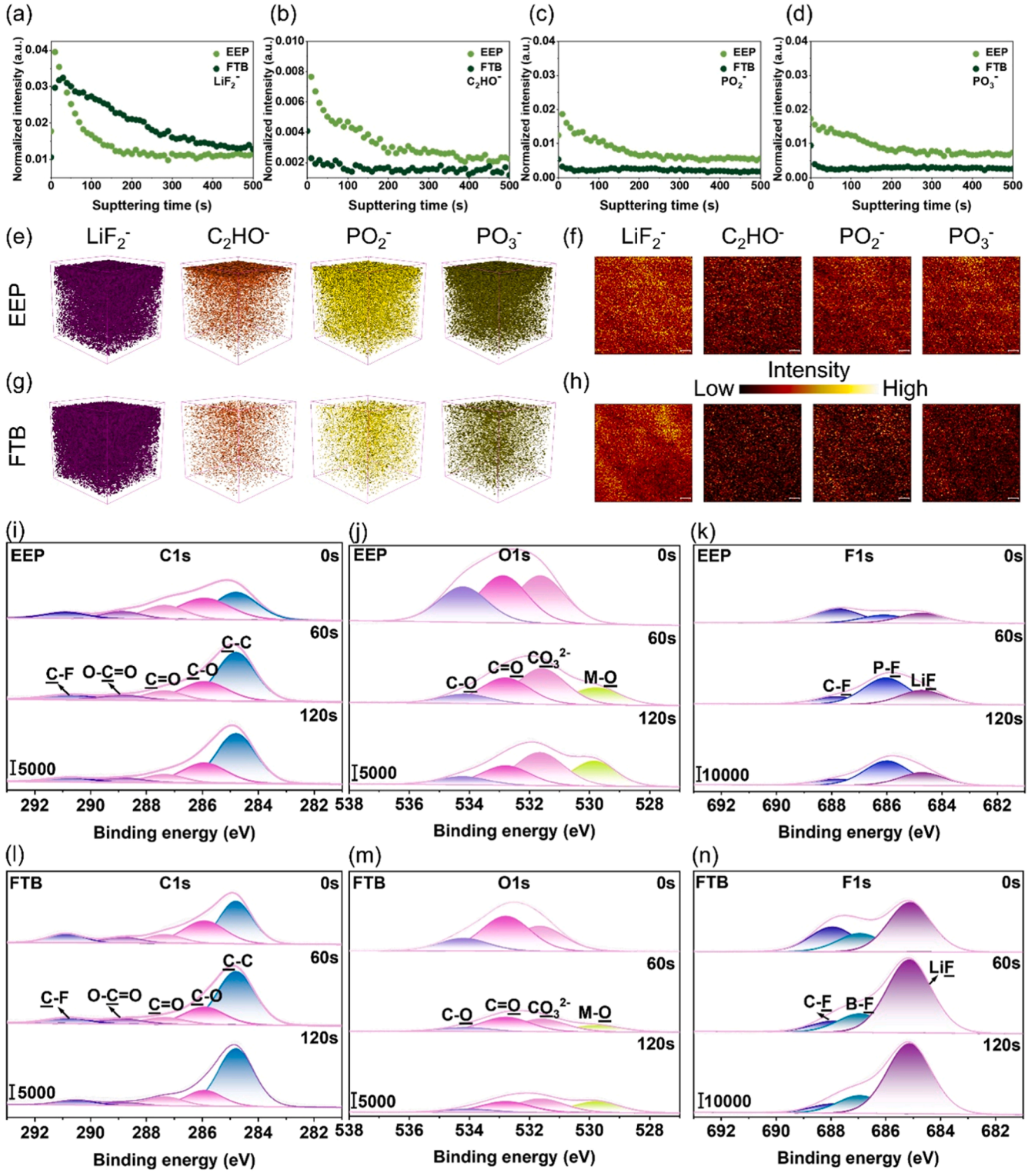

Fig. 4. Chemical characterization of the formed CEI film. TOF-SIMS depth profiles of (a) LiF_2^-, (b) C_2HO^-, (c) PO_2^- and (d) PO_3^- species. (e,g) 3D render of composition (LiF_2^-, C_2HO^-, PO_2^- and PO_3^-) and concentration distribution. (f,h) TOF-SIMS chemical imaging of LiF_2^-, C_2HO^-, PO_2^- and PO_3^- species on the surface of NMC83 tested in EEP and FTB. XPS analysis of NMC83 electrodes tested in different electrolytes, including C1s (j, l), O1s (j,m), and F1s region (k,n) with 60 seconds and 120 seconds Ar-ion etching.

the CEI surface down to the bulk material. The C 1 s spectrum of NMC83 surface after testing in EEP electrolyte (Fig. 4i,l) exposed significant peaks characteristic of C-O (286 eV) and C═O (287 eV) bonds, signifying an elevated organic solvent content. While these functional groups are pivotal for the electrolyte's solvation capacity, they may concurrently amplify the risk of decomposition in protracted cycling, adversely impacting the battery's stability and efficiency. With escalating sputtering time, the O 1 s spectrum tested in the EEP showed an increasing prevalence of CEI components dominated by C═O bonds and CO_3^{2-}, with the CO_3^{2-} peak (532 eV) (Fig. 4j, m) stemming from the

re-oxidation of alkyl carbonate, a result that engenders heightened impedance [53]. Furthermore, transition metal oxides (M-O) exhibited a distinct signal, ascribed to the corrosive effects of HF, a byproduct of the decomposition of $LiPF_6$ and carbonate solvents on the NMC83 cathode leading to the leaching of transition metals [54]. In contrast, the M-O signal in the FTB was remarkably feeble, indicative of a robust CEI film that can effectively fortify the cathode structure. A comparison of the F 1 s spectra from both electrolytes (Fig. 4k, n) reveals a prominent LiF peak at 685 eV within the FTB electrolyte, which remains consistently present throughout the entire sputtering process. This persistent peak serves as evidence for the stable presence of LiF, indicating that the FTB-based electrolyte effectively prevents the surface degradation while promoting the formation of a resilient LiF-rich CEI layer on the NMC83 surface.

2.5. Comparison of Li-ion interfacial kinetics in different electrolytes

To rigorously validate the mechanisms behind the enhanced long-term cyclability, we examined the electrochemical impedance spectroscopy (EIS) of Li||NMC83 batteries tested in EEP and FTB after

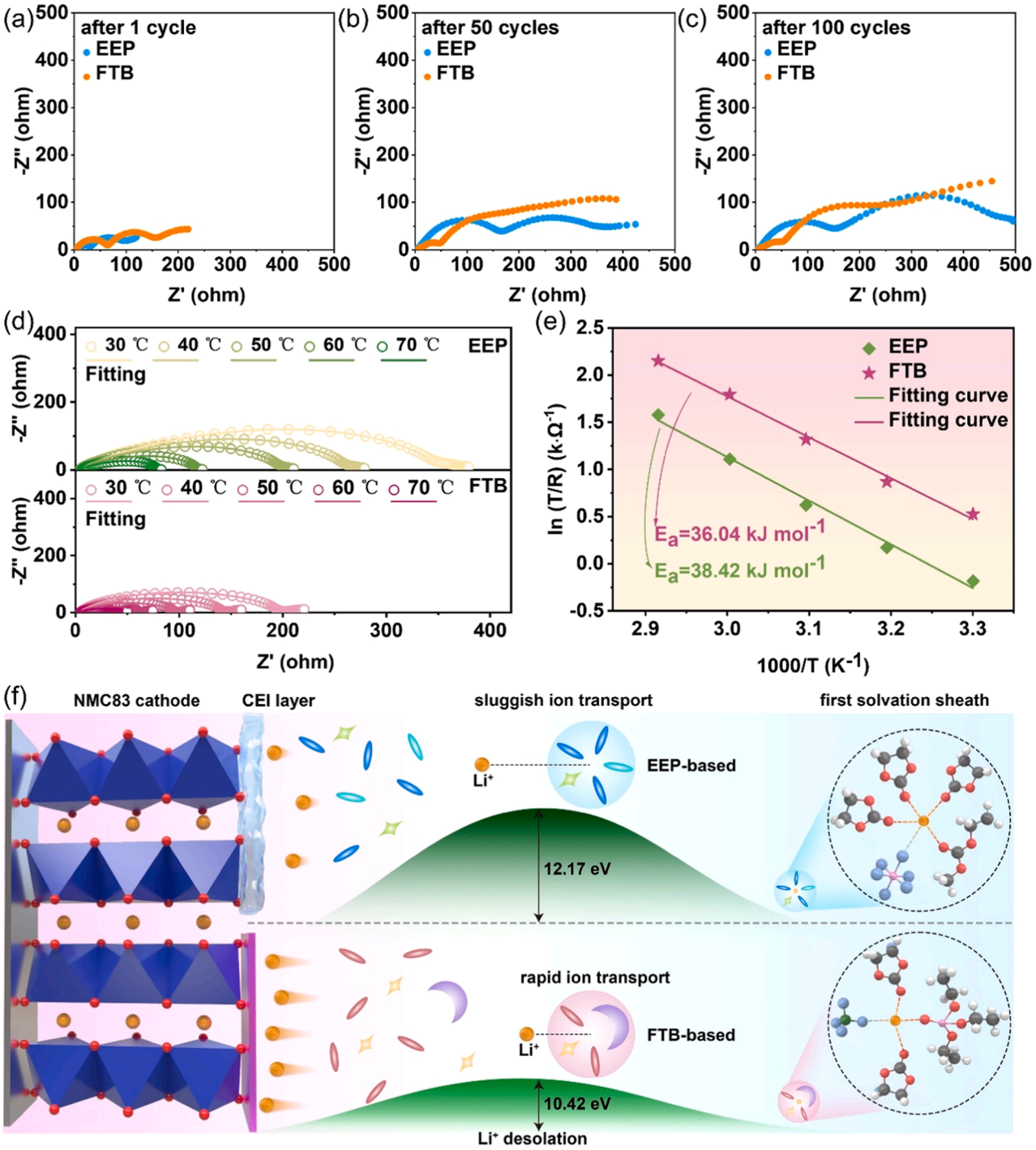

Fig. 5. Kinetics of interfacial processes near the cathode/electrolyte interface revealed by temperature-dependent EIS. (a-c) alternating current (AC) impedance spectra at different cycles in EEP and FTB electrolytes. (d) Nyquist plots of EEP-based cathode and FTB-based cathode. (e) Arrhenius plots and corresponding activation energies from Rct in Li||Li symmetrical batteries. (f) Schematic illustration of the reaction mechanism of two different electrolytes.

different cycles (Fig. 5a-c, Table S3). The semicircles in the high-frequency and medium-frequency regions can be attributed to R_{sf} and R_{ct}. It was observed that during cycling, an increment in impedance within the EEP cell precipitated a proportional escalation in overpotential and a concurrent contraction in battery capacity. The structural integrity was persistently compromised due to the substantial delithiation/lithiation of Li^+[55]. In contrast, the FTB cell initially exhibited a higher impedance; however, as the cycle count increased, the FTB-based cell demonstrated a more stable and reduced impedance, effectively preventing degradation of the cathode structure. To gain a nuanced understanding of how the designed electrolyte affects the charge transfer process in NMC83 cathodes, an extensive series of EIS tests for Li symmetric cells were conducted across temperatures ranging from 30 ℃ to 70 ℃ (Fig. 5d). It was found that FTB-based electrode consistently exhibited lower impedance than those with EEP. According to the Li^+ interaction with the electrolyte, the ions must first be desolvated from their surrounding solvent molecules [56]. The associated fitting results (Fig. 5e) indicate that the FTB-based electrolyte demands minimal activation energy for the charge transfer process, making it easier for Li^+ to participate in electrode reactions. Galvanostatic intermittent titration (GITT) measurements and the derived Li^+ diffusion coefficients (D_{Li+}) show significantly higher values for the FTB electrolyte (Fig. S9), indicating faster ion transport and better structural stability during cycling. Fig. 5f offers a stark comparison of the desolvation processes for the two electrolyte types, underscoring their distinct behaviors. The desolvation energy of quintessential solvation structures (Fig. S10) was computed, revealing that the energy for Li^+ in the EEP-based electrolyte stands at 12.17 eV, surpassing that observed within the FTB-based electrolytic framework (10.42 eV). Furthermore, Bader charge computations on solvent molecules (Fig. S11) indicate that O atoms in EC and EMC amass an incremented electron density, exhibiting heightened electronegativity, which in turn intensifies their interactive potential with Li^+. Consequently, the solvent configuration within the FEC/TEP-LBF electrolytic system enhance the kinetics of the desolvation process, leading to improved rate performance.

3. Conclusion

In conclusion, we propose a novel strategy that modulates the solvent sheath through TEP and FEC regulation. This strategy reduces the coordination number of the first shell of Li^+, resulting in a decreased energy barrier for Li^+ transport between the electrode and electrolyte, as well as enhanced charging and discharging capabilities of single-crystal NMC. Furthermore, compared to commercial electrolytes, FTB enables the formation of a LiF-rich CEI layer at the electrolyte-electrode interface. This CEI layer effectively suppresses structural damage to the single-crystal cathode, mitigates the detrimental oxidative decomposition, and prevents the dissolution of transition metals. The excellent interfacial compatibility is demonstrated by the enhanced discharge capacities at different current densities (~209 mAh g^{-1} at 0.1 C and ~192 mAh g^{-1} at 0.5 C) and an impressive capacity retention of 88.2 % in Li||NMC83 batteries after 300 cycles at 1 C, corresponding to a discharge capacity of 169.2 mAh g^{-1}. This approach to solvent sheath modulation presents a pioneering direction for the development of energy storage systems that offer both high energy density and enhanced safety, thus paving the way for the next generation high-performance single-crystal based lithium batteries.

CRediT authorship contribution statement

Lingli Chen: Conceptualization, Methodology, Formal analysis, Characterization of samples, Writing – original draft. **Biwei Xiao:** Data curation, Validation. **Weibin Chen:** Formal analysis, Visualization. **Pengtao Zhang:** Resources, Investigation. **Tao Huang:** Supervision, Data curation. **Weiyuan Huan:** Formal analysis, supervision. **Zhencheng Huang:** Project administration, Software. **Qingyun Lin:** Software, Resources. **Pei Liu:** Validation, Investigation. **Xuanlong He:** Data curation, Validation. **Yuying Liu:** Methodology, Visualization. **Haoran Wei:** Software, Resources. **Shenghua Ye:** Data curation, Formal analysis. **Liewu Li:** Investigation, Methodology. **Jing Chen:** Software, Resources. **Xuming Yang:** Project administration, Supervision. **Xiangzhong Ren:** Writing – review & editing. **Xiaoping Ouyang:** Writing – review & editing. **Jianhong Liu:** Supervision. **Feng Pan:** Writing – review & editing, Project administration. **Qianling Zhang:** Supervision, Project administration, Writing – review & editing. **Jiangtao Hu:** Supervision, Project administration, Writing – review & editing.

Declaration of Competing Interest

The authors declare that they have no known competing financial interests or personal relationships that could have appeared to influence the work reported in this paper.

Data availability

Data will be made available on request.

Acknowledgements

This work has been financially backed by Shenzhen Science and Technology Program (No. KJZD20230923115005009), National Natural Science Foundation (NNSF) of China (No. 52202269). Additionally, we have received support from the Shenzhen Science and Technology program (No. 20220810155330003), Basic and Applied Basic Research Foundation of Guangdong Province (No. 2021B1515130002) and Xiangjiang Lab (No. 22XJ01007). In addition, we gratefully acknowledge the financial support of Project of Department of Education of Guangdong Province (No. 2022ZDZX3018). We extend our thanks to the Instrumental Analysis Center at Shenzhen University's Xili Campus for supplying the necessary facilities for our material analysis.

Appendix A. Supporting information

Supplementary data associated with this article can be found in the online version at doi:10.1016/j.nanoen.2024.110276.

References

[1] H. Wan, J. Xu, C. Wang, Designing electrolytes and interphases for high-energy lithium batteries, Nat. Rev. Chem. 8 (2024) 30–44.
[2] Q. Wang, T. O'Carroll, F. Shi, Y. Huang, G. Chen, X. Yang, A. Nevar, N. Dudko, N. Tarasenko, J.J.E.E.R. Xie, Designing organic material electrodes for lithium-ion batteries: progress, challenges, and perspectives, Electrochem. Energy Rev. 7 (2024) 15.
[3] X. Chen, X. Yin, J. Aslam, W. Sun, Y.J.E.E.R. Wang, Recent progress and design principles for rechargeable lithium organic batteries, Electrochem. Energy Rev. 5 (2022) 12.
[4] M.M. Thackeray, K. Amine, Layered Li–Ni–Mn–Co oxide cathodes, Nat. Energy 6 (2021) 933. -933.
[5] J. Zheng, Y. Ye, F. Pan, Structure units' as material genes in cathode materials for lithium-ion batteries, Natl. Sci. Rev. 7 (2020) 242–245.
[6] A. Manthiram, A reflection on lithium-ion battery cathode chemistry, Nat. Commun. 11 (2020) 1550.
[7] W. Li, E.M. Erickson, A. Manthiram, High-nickel layered oxide cathodes for lithium-based automotive batteries, Nat. Energy 5 (2020) 26–34.
[8] J. Hu, L. Li, Y. Bi, J. Tao, J. Lochala, D. Liu, B. Wu, X. Cao, S. Chae, C. Wang, Locking oxygen in lattice: a quantifiable comparison of gas generation in polycrystalline and single crystal Ni-rich cathodes, Energy Storage Mater. 47 (2022) 195–202.
[9] J. Hu, L. Li, E. Hu, S. Chae, H. Jia, T. Liu, B. Wu, Y. Bi, K. Amine, C. Wang, Mesoscale-architecture-based crack evolution dictating cycling stability of advanced lithium ion batteries, Nano Energy 79 (2021) 105420.
[10] Y. Bi, J. Tao, Y. Wu, L. Li, Y. Xu, E. Hu, B. Wu, J. Hu, C. Wang, J.-G. Zhang, Reversible planar gliding and microcracking in a single-crystalline Ni-rich cathode, Science 370 (2020) 1313–1317.
[11] L. Ni, S. Zhang, A. Di, W. Deng, G. Zou, H. Hou, X. Ji, Challenges and strategies towards single-crystalline Ni-rich layered cathodes, Adv. Energy Mater. 12 (2022) 2201510.

[12] H. Zhang, X. He, Z. Chen, Y. Yang, H. Xu, L. Wang, X. He, Single-crystalline Ni-rich LiNixMnyCo1− x− yO2 cathode materials: a perspective, Adv. Energy Mater. 12 (2022) 2202022.
[13] X. Ou, T. Liu, W. Zhong, X. Fan, X. Guo, X. Huang, L. Cao, J. Hu, B. Zhang, Y. S. Chu, Enabling high energy lithium metal batteries via single-crystal Ni-rich cathode material co-doping strategy, Nat. Commun. 13 (2022) 2319.
[14] W. Wang, Y. Zhou, B. Zhang, W. Huang, L. Cheng, J. Wang, X. He, L. Yu, Z. Xiao, J. Wen, Optimized in situ doping strategy stabling single-crystal ultrahigh-nickel layered cathode materials, ACS Nano 18 (2024) 8002–8016.
[15] Z. Zhang, B. Hong, M. Yi, X. Fan, Z. Zhang, X. Huang, Y. Lai, In situ co-doping strategy for achieving long-term cycle stability of single-crystal Ni-rich cathodes at high voltage, Chem. Eng. J. 445 (2022) 136825.
[16] X.M. Fan, Y.D. Huang, H.X. Wei, L.B. Tang, Z.J. He, C. Yan, J. Mao, K.H. Dai, J. C. Zheng, Surface modification engineering enabling 4.6 V single-crystalline Ni-rich cathode with superior long-term cyclability, Adv. Funct. Mater. 32 (2022) 2109421.
[17] L. Wang, T. Liu, T. Wu, J. Lu, Strain-retardant coherent perovskite phase stabilized Ni-rich cathode, Nature 611 (2022) 61–67.
[18] P. Yan, J. Zheng, J. Liu, B. Wang, X. Cheng, Y. Zhang, X. Sun, C. Wang, J.-G. Zhang, Tailoring grain boundary structures and chemistry of Ni-rich layered cathodes for enhanced cycle stability of lithium-ion batteries, Nat. Energy 3 (2018) 600–605.
[19] S. Tan, Z. Shadike, J. Li, X. Wang, Y. Yang, R. Lin, A. Cresce, J. Hu, A. Hunt, I. Waluyo, Additive engineering for robust interphases to stabilize high-Ni layered structures at ultra-high voltage of 4.8 V, Nat. Energy 7 (2022) 484–494.
[20] S. Chen, G. Zheng, X. Yao, J. Xiao, W. Zhao, K. Li, J. Fang, Z. Jiang, Y. Huang, Y.J. An Ji, Constructing matching cathode–anode interphases with improved chemo-mechanical stability for high-energy batteries, ACS Nano 18 (8) (2024) 6600–6611.
[21] H. Cheng, Q. Sun, L. Li, Y. Zou, Y. Wang, T. Cai, F. Zhao, G. Liu, Z. Ma, W. Wahyudi, Emerging era of electrolyte solvation structure and interfacial model in batteries, ACS Energy Lett. 7 (2022) 490–513.
[22] Z. Piao, R. Gao, Y. Liu, G. Zhou, H.M. Cheng, A review on regulating Li+ solvation structures in carbonate electrolytes for lithium metal batteries, Adv. Mater. 35 (2023) 2206009.
[23] X. Li, X. Han, G. Li, J. Du, Y. Cao, H. Gong, H. Wang, Y. Zhang, S. Liu, B. Zhang, Nonsacrificial nitrile additive for armoring high-voltage LiNi0. 83Co0. 07Mn0. 1O2 cathode with reliable electrode–electrolyte interface toward durable battery, Small 18 (2022) 2202989.
[24] G.A. Giffin, The role of concentration in electrolyte solutions for non-aqueous lithium-based batteries, Nat. Commun. 13 (2022) 5250.
[25] J. Hu, W. Li, Y. Duan, S. Cui, X. Song, Y. Liu, J. Zheng, Y. Lin, F. Pan, Single-particle performances and properties of LiFePO4 nanocrystals for Li-Ion batteries, Adv. Energy Mater. 7 (2017) 1601894.
[26] D. Lu, R. Li, M.M. Rahman, P. Yu, L. Lv, S. Yang, Y. Huang, C. Sun, S. Zhang, H. Zhang, Ligand-channel-enabled ultrafast Li-ion conduction, Nature (2024) 1–7.
[27] Z. Deng, Y. Jia, Y. Deng, C. Xu, X. Zhang, Q. He, J. Peng, H. Wu, W. Cai, Coordination structure regulation in non-flammable electrolyte enabling high voltage lithium electrochemistry, J. Energy Chem. 15 (2024) 1–7.
[28] C.-Y. Wang, T. Liu, X.-G. Yang, S. Ge, N.V. Stanley, E.S. Rountree, Y. Leng, B. D. McCarthy, Fast charging of energy-dense lithium-ion batteries, Nature 611 (2022) 485–490.
[29] J. Xing, S. Bliznakov, L. Bonville, M. Oljaca, R.J.E.E.R. Maric, A review of nonaqueous electrolytes, binders, and separators for lithium-ion batteries, Electrochem. Energy Rev. 5 (2022) 14.
[30] S. Zhang, S. Li, Y. Lu, Designing safer lithium-based batteries with nonflammable electrolytes: a review, eScience 1 (2021) 163–177.
[31] W. Tu, P. Xia, X. Zheng, C. Ye, M. Xu, W. Li, Insight into the interaction between layered lithium-rich oxide and additive-containing electrolyte, J. Power Sources 341 (2017) 348–356.
[32] Z. Wang, R. Han, H. Zhang, D. Huang, F. Zhang, D. Fu, Y. Liu, Y. Wei, H. Song, Y. Shen, An intrinsically nonflammable electrolyte for prominent-safety lithium metal batteries with high energy density and cycling stability, Adv. Funct. Mater. 33 (2023) 2215065.
[33] C. Zu, H. Yu, H. Li, Enabling the thermal stability of solid electrolyte interphase in Li-ion battery, InfoMat 3 (2021) 648–661.
[34] S. Li, S. Zhang, S. Chai, X. Zang, C. Cheng, F. Ma, L. Zhang, Y. Lu, Structured solid electrolyte interphase enable reversible Li electrodeposition in flame-retardant phosphate-based electrolyte, Energy Storage Mater. 42 (2021) 628–635.
[35] S. Zhang, S. Li, X. Wang, C. Li, Y. Liu, H. Cheng, S. Mao, Q. Wu, Z. Shen, J.J.N. E. Mao, Nonflammable electrolyte with low exothermic design for safer lithium-based batteries, Nano Energy 114 (2023) 108639.
[36] S. Chen, Z. Wang, H. Zhao, H. Qiao, H. Luan, L.J.Jo.P.S. Chen, A novel flame retardant and film-forming electrolyte additive for lithium ion batteries, J. Power Sources 187 (2009) 229–232.
[37] J. Wang, Z. Zhang, J. Han, X. Wang, L. Chen, H. Li, F.J.N.E. Wu, Interfacial and cycle stability of sulfide all-solid-state batteries with Ni-rich layered oxide cathodes, Nano Energy 100 (2022) 107528.
[38] H. Huang, J. Jin, C. Zheng, L. Wang, H. Yuan, T. Xiu, Z. Song, M.E. Badding, K. Yue, X.J.A.F.M. Tao, Bonded interface enabled durable solid-state lithium metal batteries with ultra-low interfacial resistance of 0.25 Ω cm2, Adv. Funct. Mater. (2024) 2407619.
[39] W.C. Zheng, Z. Huang, C.G. Shi, Y. Deng, Z.H. Wen, Z. Li, H. Chen, Z. Chen, L. Huang, S.G.J.C. Sun, Interphase engineering for stabilizing Ni-rich cathode in lithium-ion batteries by a nucleophilic reaction-based additive, ChemSusChem 16 (2023) 202202252.
[40] C. Liu, C. Miao, Z. Li, S. Nie, Z. Yi, W.J.C.E.J. Xiao, Revealing the origin of enhanced structural stability for nickel-rich LiNi0. 83Co0. 11Mn0. 06O2 cathodes in situ modified with multifunctional polysiloxane, Chem. Eng. J. 491 (2024) 152078.
[41] Q. Zhang, Q. Deng, W. Zhong, J. Li, Z. Wang, P. Dong, K. Huang, C.J.A.F.M. Yang, Tungsten boride stabilized single-crystal LiNi0. 83Co0. 07Mn0. 1O2 cathode for high energy density lithium-ion batteries: performance and mechanisms, Adv. Funct. Mater. 33 (2023) 2301336.
[42] X.-H. Meng, T. Lin, H. Mao, J.-L. Shi, H. Sheng, Y.-G. Zou, M. Fan, K. Jiang, R.-J. Xiao, D.J.JotA.C.S. Xiao, Kinetic origin of planar gliding in single-crystalline Ni-rich cathodes, J. Am. Chem. Soc. 144 (2022) 11338–11347.
[43] S. Zhang, X. Zhou, S. Li, Z. Feng, X. Fan, D. Sun, H. Wang, Y.J.M.C.F. Tang, Construction of a nickel-rich LiNi 0.83 Co 0.11 Mn 0.06 O 2 cathode with high stability and excellent cycle performance through interface engineering, Mater. Chem. Front. 7 (2023) 490–501.
[44] G. Yu, B. Luo, S. Su, Q. Wang, W. Ji, D. Peng, Z. Liu, X. Wang, Z. Zhao, J.J.A.S. C. Zhang, Engineering, inverse spinel-structured Mg2MnO4 coating to enable superior thermal stability of LiNi0. 83Co0. 12Mn0. 05O2 cathodes for lithium-ion batteries, ACSSustainable Chem. Eng. 11 (2023) 15282–15293.
[45] J. Pan, H. Yuan, J. Wu, M. Li, X. Wu, W. Zeng, Z. Wen, R.J.S. Qian, Anion-dominated solvation in low-concentration electrolytes promotes inorganic-rich interphase formation in lithium metal batteries, Small (2024) 2404260.
[46] J. Zhao, M. Li, H. Su, Y. Liu, P. Bai, H. Liu, L. Ma, W. Li, J. Sun, Y.J.S.M. Xu, In situ fabricated non-flammable quasi-solid electrolytes for Li-metal batteries, Small Methods 7 (2023) 2300228.
[47] Z. Piao, X. Wu, H.-R. Ren, G. Lu, R. Gao, G. Zhou, H.-M. Cheng, A semisolvated sole-solvent electrolyte for high-voltage lithium metal batteries, J. Am. Chem. Soc. 145 (2023) 24260–24271.
[48] P. Yan, J. Zheng, M. Gu, J. Xiao, J.-G. Zhang, C.-M.J.Nc Wang, Intragranular cracking as a critical barrier for high-voltage usage of layer-structured cathode for lithium-ion batteries, Nat. Commun. 8 (2017) 14101.
[49] F.B. Spingler, S. Kücher, R. Phillips, E. Moyassari, A.J.Jo.T.E.S. Jossen, Electrochemically stable in situ dilatometry of NMC, NCA and graphite electrodes for lithium-ion cells compared to XRD measurements, J. Electrochem. Soc. 168 (2021) 040515.
[50] X. He, J. Shen, B. Zhang, Z. Xiao, L. Ye, Q. Mao, Q. Zhong, X. Ou, Surface Li+/Ni2+ antisite defects construction for achieving high-voltage stable single-crystal Ni-rich cathode by anion/cation Co-doping, Adv. Funct. Mater. (2024) 2401300.
[51] Z. Dai, Z. Li, R. Chen, F. Wu, L. Li, Defective oxygen inert phase stabilized high-voltage nickel-rich cathode for high-energy lithium-ion batteries, Nat. Commun. 14 (2023) 8087.
[52] K. Kim, D. Hwang, S. Kim, S.O. Park, H. Cha, Y.S. Lee, J. Cho, S.K. Kwak, N.S. Choi, Cyclic aminosilane-based additive ensuring stable electrode–electrolyte interfaces in Li-ion batteries, Adv. Energy Mater. 10 (2020) 2000012.
[53] H. Su, Z. Chen, M. Li, P. Bai, Y. Li, X. Ji, Z. Liu, J. Sun, J. Ding, M. Yang, Achieving practical high-energy-density lithium-metal batteries by a dual-anion regulated electrolyte, Adv. Mater. 35 (2023) 2301171.
[54] Y. Zou, K. Zhou, G. Liu, N. Xu, X. Zhang, Y. Yang, J. Zhang, J. Zheng, Enhanced cycle life and rate capability of single-crystal, Ni-Rich LiNi0. 9Co0. 05Mn0. 05O2 enabled by 1, 2, 4–1 H-triazole additive, ACS Appl. Mater. Interfaces 13 (2021) 16427–16436.
[55] D. Ouyang, J. Weng, M. Chen, J. Wang, Z. Wang, Investigation on topographic, electrochemical and thermal features of aging lithium-ion cells induced by overcharge/over-discharge cycling, J. Energy Storage 68 (2023) 107799.
[56] E. Barsoukov, D. Kim, H.-S. Lee, H. Lee, M. Yakovleva, Y. Gao, J.F.J.S.S.I. Engel, Comparison of kinetic properties of LiCoO2 and LiTi0. 05Mg0. 05Ni0. 7Co0. 2O2 by impedance spectroscopy, Solid State Ion. 161 (2003) 19–29.